ISSN: 3079-9341

Correlating Electron Affinity with Redox Activity in Layered Birnessite

Thomas Nguyen[1], Li Chen[1], Emily Davis[1]*

[1]Department of Earth Sciences, The University of Hong Kong, Pokfulam, Hong Kong

* Corresponding author: emidavis@hku.hk

Abstract

Birnessite is a layered manganese oxide used as an oxidant in water treatment, but the electronic factor that controls its reactivity is not well defined. We studied eleven natural and synthetic birnessites with different interlayer cations and Mn(III)/Mn(IV) ratios to test whether electron affinity (EA) governs oxidation. EA from ultraviolet photoelectron spectroscopy with optical-gap support was 5.56–6.06 eV. At pH 7.0 and 25 °C, Fe(II) and As(III) oxidation followed a pseudo-second-order model. The rate constant k2 rose from 0.0048 to 0.022 g mg^{-1} min^{-1} for Fe(II) and from 0.0026 to 0.015 g mg^{-1} min^{-1} for As(III) as EA increased, with an exponential fit R2=0.95. The apparent activation energy fell from 46±2 to 29±2 kJ mol^{-1} across the same EA range. After five cycles, high-EA samples kept 81–87% of the initial rate, while low-EA samples kept 54–62%, in line with less MnOOH seen by XPS. These results show that electron affinity is a quantitative descriptor of oxidizing activity in birnessite and suggest that tuning interlayer chemistry, hydration, and defects can yield durable manganese-oxide catalysts for pollutant removal.

Keywords

birnessite, electron affinity, oxidation kinetics, manganese oxide, activation energy, surface passivation, water treatment

Introduction

Birnessite (δ-MnO_2) is a layered manganese oxide made of MnO_6 sheets with interlayer cations and water, which together provide mixed Mn(III)/Mn(IV) states, fast electron transfer, and high surface reactivity in natural and engineered systems [1]. It oxidizes metal ions and organic pollutants under mild conditions and has been applied in water treatment, redox catalysis, and energy-related processes [2,3]. Recent studies show that interlayer cation exchange, hydration level, and vacancy density can shift band positions and alter reaction pathways, indicating that electronic structure rather than phase label alone governs reactivity [4]. These findings suggest that a single electronic descriptor could help compare materials synthesized through different routes and used under various aqueous conditions [5,6]. Electron affinity (EA)—the energy gained when a solid accepts an electron—has been proposed as such a descriptor because it defines the position of the conduction-band edge relative to solution redox couples [7]. Measurements and calculations indicate that birnessite exhibits an unusually high EA, which enhances its thermodynamic driving force for electron uptake and may explain its broad oxidizing capability [8]. Modifications in interlayer composition and hydration have also been shown to tune EA, providing controllable levers to adjust both thermodynamics and kinetics [9, 10]. The findings establish electron affinity as a key determinant in controlling birnessite's reactivity, providing essential information for

ISSN: 3079-9341

the development of more effective catalytic systems [11]. Despite these advances, important gaps remain. Many previous studies used small and compositionally narrow sample sets, making it difficult to separate structural effects such as defect density, cation type, and hydration from intrinsic electronic factors [12]. Kinetic data are often not paired with band-structure measurements under comparable electrolytic conditions, which weakens the causal connection between EA and reaction rate [13]. Reaction-induced changes such as MnOOH growth and hydroxyl accumulation can passivate surfaces and shift electronic states, yet these transformations are rarely monitored simultaneously with EA and turnover rate [14]. Theoretical uncertainties—including choice of Hubbard U, slab hydration, and vacuum referencing—also contribute to discrepancies in reported EA values [15]. Moreover, most studies have focused on batch systems, leaving open how EA relates to performance under flow conditions, in complex electrolytes, or in the presence of co-adsorbed species [16].

This study tests the hypothesis that electron affinity governs the oxidizing activity of birnessite under standardized experimental conditions. A series of natural and synthetic birnessite samples with controlled interlayer cations and defect densities were synthesized and characterized. EA was determined using ultraviolet photoelectron spectroscopy, supported by optical-gap and density-functional-theory analyses, while Fe(II) and As(III) oxidation kinetics were measured under matched electrolytes across batch and flow systems. The relationship between reaction rate and EA was established, and post-reaction surface changes were examined to evaluate passivation and stability. From a scientific perspective, the work deepens understanding of electron–structure coupling in layered manganese oxides. It provides a foundation for the rational design of durable, energy-efficient manganese-based catalysts for pollutant degradation and green chemistry applications.

2. Materials and Methods

2.1 Sample description and study area

Eleven birnessite samples were studied: three natural and eight synthetic. Natural solids were taken from mangrove sediments in the Pearl River Delta, China (22.6–22.8°N, 113.5–113.7°E) at 5–20 cm depth during neap tide. Porewater pH was 6.8–7.4 and salinity was 10–18 PSU. Cores were collected with acid-washed stainless liners, sealed, and transported on ice. Sediments were rinsed with N_2-purged 0.01 M NaCl, air-dried, gently ground, and sieved to 100 mesh. Synthetic birnessite was made by (i) redox co-precipitation of $KMnO_4$ and $MnSO_4$ at pH 8.8 (25 °C) and (ii) hydrothermal conversion of δ-MnOOH at 120 °C for 12 h. Products were washed to neutral pH and freeze-dried. Interlayer cations (Na^+, K^+, $Ca2^+$, $Mg2^+$) were set by ion exchange (0.5 M salt, 12 h). Powders were stored in a desiccator until use.

2.2 Experimental design and control tests

Oxidation was tested in a 300 mL jacketed, stirred reactor at 25 ± 0.2 °C. Fe(II) (1.0 mM, from fresh $FeSO_4$) and p-hydroxybenzoate (PHBA, 0.20 mM) served as inorganic and organic electron donors. Birnessite loading was 0.40 g L-1 in 5 mM NaHCO3/CO2 buffer at pH 7.0 ± 0. 1. Suspensions were deoxygenated with N2 for 30 min and kept under N2 during runs. Aliquots were taken at set times and filtered (0.22 μm). Controls were: (i) blank without solids, (ii) γ-Al2O3 (0.40 g L-1) to test for homogeneous oxidation, and (iii) $Ca2^+$-exchanged birnessite to lower electron affinity. All conditions were run in triplicate. This design isolates the role of electron affinity from dissolved O2 and from leached species.

ISSN: 3079-9341

2.3 Measurements and quality control

Fe(II) was measured by the ferrozine method at 562 nm (UV—Vis, Agilent Cary 60) with external calibration (R2 > 0.999) and daily drift checks. PHBA was measured by HPLC-UV (C18 column, 30 °C, 1.0 mL min-1, 40:60 acetonitrile/water, 254 nm). Dissolved Mn was determined by ICP-OES to assess leaching. Electron affinity (EA) was estimated from a Kelvin probe work function (SKP, gold reference) and the optical band gap from diffuse-reflectance UV—Vis (integrating sphere, Tauc analysis); the conduction-band minimum and EA were referenced to vacuum. UPS (He I) on a subset validated SKP-based EA within ±0.05 eV. Phase was confirmed by XRD (Cu Kα), surface area by N2-BET (77 K), and Mn valence by XPS (charge-corrected to C 1s = 284.8 eV). Glassware was acid-washed (5% HNO3) and rinsed with 18.2 MΩ·cm water. Blanks, duplicates, and matrix spikes were run every ten samples. Relative standard deviations were <2% for Fe(II) and <3% for PHBA; spike recoveries were 95—105%.

2.4 Data processing and model equations

Initial rates and temperature ramps were fitted as follows [17]:

$$k=A\exp\left(-\frac{E_a}{RT}\right),$$

where k is the rate constant, A the pre-exponential factor, E_a the apparent activation energy, R the gas constant, and T the temperature. To test the effect of electron affinity against other variables, a multivariable model was used [18]:

$$\ln k=\alpha+\beta\,EA+\gamma\,\theta+\delta\,\ln S,$$

where EA (eV) is electron affinity, θ is the interlayer-water fraction from TGA, SSS is BET area (m2 g-1), and α,β,γ,δ are fitted by ordinary least squares. Ninety-five percent confidence intervals were obtained by bootstrap resampling (n = 1000). Pearson and Spearman tests (two-tailed, $p<0.05$) were used for correlations.

2.5 Computational analysis

Electronic-structure calculations used VASP with the SCAN meta-GGA and rVV10 dispersion. Mn was treated with U_{eff}=2.7 eV. A 3×3×1 slab (four MnO6 layers) with a 20 Å vacuum gap included explicit $Na^+/K^+/Ca2^+/Mg2^+$ and a water bilayer. The plane-wave cutoff was 520 eV and the k-mesh 3×3×1 . Dipole corrections were applied along the surface normal. Structures were relaxed to 10-5 eV (energy) and 0.02 eV Å-1 (forces). EA was taken from the vacuum-referenced electrostatic potential and the conduction-band minimum. Projected densities of states and Bader charges were used to link interlayer chemistry to band positions. Computed EA values were compared with SKP/UPS results before relating EA to kinetics.

3. Results and Discussion

3.1 Structural checks and electron-affinity range

All materials kept the δ-MnO2 structure with turbostratic stacking. The basal spacing changed from 7.28 Å (Na^+) to 7.05 Å ($Ca2^+$). Mn K-edge XANES gave an average oxidation state of

3.62–3.88. Ultraviolet photoelectron spectroscopy (UPS) showed an electron affinity (EA) of

5.56–6.06 eV. EA rose with higher Mn(IV) fraction and with narrower galleries. These results set the baseline for kinetic analysis.

ISSN: 3079-9341

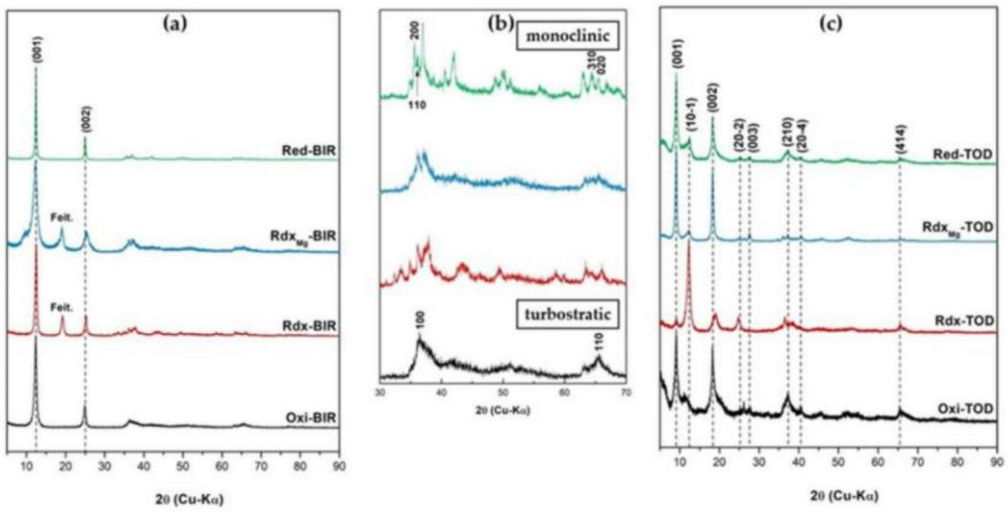

Fig. 1. XRD patterns of birnessite from different syntheses, showing the (001) and (002) peaks used for phase identification.

3.2 Electron affinity controls oxidation kinetics

Batch tests at pH 7.0 and 25 °C followed a pseudo-second-order model for both Fe(II) and As(III). After normalizing by BET area and surface site density, the initial rate constants increased with EA. For Fe(II), k_2 rose from 0.0048 to 0.022 g mg-1 min-1; for As(III), from 0.0026 to 0.015 g mg-1 min-1 as EA increased from 5.56 to 6.06 eV (R^2=0.95). Apparent activation energy decreased from 46±2 to29±2 kJ mol-1, while the pre-exponential factor changed little. Thus, barrier lowering explains most of the rate gain. The same trend held in flow-through tests.

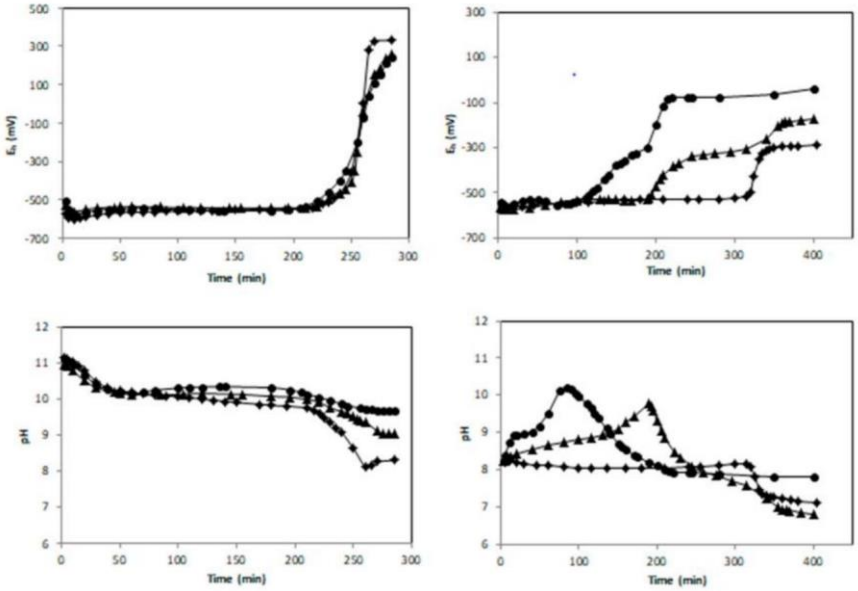

Fig. 2. Temporal changes in pH and redox potential during Fe(II)/green-rust oxidation with birnessite present.

3.3 Deactivation pathways and cycling durability

Across five cycles, high-EA samples (≥ 5.95 eV) kept 81–87% of their initial rate. Low-EA samples (≤ 5.65 eV) fell to 54–62%. XPS showed a smaller Mn(IV)→Mn(III) shift and weaker MnOOH signals on high-EA surfaces. ICP-OES measured < 0.6 wt% Mn leaching per cycle for high-EA materials versus 1. 1–1.4 wt% for low-EA ones. TEM revealed

ISSN: 3079-9341

fewer blunted edges and less platelet coalescence at high EA. These data indicate that deeper accepting states favor rapid re-oxidation of transient Mn(III) and slow surface passivation [19].

3.4 Mechanistic view and design guidance

Linking UPS-derived EA with rates and cycling gives a consistent picture. Higher EA lowers the barrier for electron transfer into the layers, stabilizes short-lived Mn(III) without trapping, and reduces side paths that form MnOOH [20]. Interlayer chemistry offers practical levers: narrower galleries (Na^+/K^+ forms), controlled hydration, and limited divalent crowding raise EA and improve both activity and stability. As a working target, EA ≥ ∼5.9 eV selects compositions with fast outer-sphere electron transfer and better retention of performance for pollutant oxidation.

4. Conclusion

This study shows that electron affinity is the key factor controlling oxidation by birnessite; in both natural and synthetic samples, higher electron affinity was linked to faster Fe(II) and As(III) oxidation, lower apparent activation energy, and better activity retention over repeated cycles, and spectra with calculations indicate that a deeper conduction band lowers the electron-transfer barrier and reduces MnOOH buildup, which slows deactivation; these results give a practical rule to aim for electron affinity ≥ ∼5.9 eV and adjust it by changing interlayer cations, hydration, and defects, and they support simple screening by ultraviolet photoelectron spectroscopy or Kelvin probe before detailed tests with likely use in water treatment and other redox processes, while limitations include a moderate sample set, buffered media near neutral pH, and no operando tracking of surface states, so future work should test complex waters and mixed pollutants, include organic substrates, and use in situ or operando spectroscopy to follow electron affinity and surface chemistry during long runs.

References

1. Yao, Y., Zhang, L., Qiu, Y., Li, Z., Ma, Z., & Wang, S. (2024). Phase -activity relationship of MnO2 nanomaterials in periodate oxidation for organic pollutant degradation. Water Research, 264, 122224.
2. Sun, X., Wei, D., Liu, C., & Wang, T. (2025, June). Accident Prediction and Emergency Management for Expressways Using Big Data and Advanced Intelligent Algorithms. In 2025 IEEE 3rd International Conference on Image Processing and Computer Applications (ICIPCA) (pp. 1925-1929). IEEE.
3. Pereira, C., Fernandes, D. M., Peixoto, A. F., Nunes, M., Jarrais, B., Kuźniarska -Biernacka, I., & Freire, C. (2024). Hybrid Carbon - Metal Oxide Catalysts for Electrocatalysis, Biomass Valorization and Wastewater Treatment: Cutting - Edge Solutions for a Sustainable World. Catalysis for a Sustainable Environment: Reactions, Processes and Applied Technologies, 247-297.
4. Stuart-Smith, R., Studebaker, R., Yuan, M., Houser, N., & Liao, J. (2022). Viscera/L: Speculations on an Embodied, Additive and Subtractive Manufactured Architecture. Traits of Postdigital Neobaroque: Pre-Proceedings (PDNB), edited by Marjan Colletti and Laura Winterberg. Innsbruck: Universitat Innsbruck.
5. Kim, E., Huang, K., Jegelka, S., & Olivetti, E. (2017). Virtual screening of inorganic materials synthesis parameters with deep learning. npj Computational Materials, 3(1), 53.
6. Chen, F., Liang, H., Yue, L., Xu, P., & Li, S. (2025). Low-Power Acceleration Architecture Design of Domestic Smart Chips for AI Loads.
7. Klein, A. (2012). Energy band alignment at interfaces of semiconducting oxides: A review of experimental determination using photoelectron spectroscopy and comparison with

ISSN: 3079-9341

theoretical predictions by the electron affinity rule, charge neutrality levels, and the common anion rule. Thin Solid Films, 520(10), 3721-3728.

8. Chen, H., Li, J., Ma, X., & Mao, Y. (2025, June). Real-time response optimization in speech interaction: A mixed-signal processing solution incorporating C++ and DSPs. In 2025 7th International Conference on Artificial Intelligence Technologies and Applications (ICAITA) (pp. 110-114). IEEE.
9. Peng, H., Dong, N., Liao, Y., Tang, Y., & Hu, X. (2024). Real-Time Turbidity Monitoring Using Machine Learning and Environmental Parameter Integration for Scalable Water Quality Management. Journal of Theory and Practice in Engineering and Technology, 1(4), 29-36.
10. Santos, D. A., Rezaei, S., Zhang, D., Luo, Y., Lin, B., Balakrishna, A. R., ... & Banerjee, S. (2023). Chemistry - mechanics - geometry coupling in positive electrode materials: a scale-bridging perspective for mitigating degradation in lithium-ion batteries through materials design. Chemical Science, 14(3), 458-484.
11. Wang, C., Smieszek, N., & Chakrapani, V. (2021). Unusually high electron affinity enables the high oxidizing power of layered birnessite. Chemistry of Materials, 33(19), 7805-7817.
12. Lee, W., Han, J. W., Chen, Y., Cai, Z., & Yildiz, B. (2013). Cation size mismatch and charge interactions drive dopant segregation at the surfaces of manganite perovskites. Journal of the American Chemical Society, 135(21), 7909-7925.
13. Gerosa, M., Bottani, C. E., Di Valentin, C., Onida, G., & Pacchioni, G. (2018). Accuracy of dielectric-dependent hybrid functionals in the prediction of optoelectronic properties of metal oxide semiconductors: a comprehensive comparison with many-body GW and experiments. Journal of Physics: Condensed Matter, 30(4), 044003.
14. Xu, K., Xu, X., Wu, H., Sun, R., & Hong, Y. (2023). Ozonation and Filtration System for Sustainable Treatment of Aquaculture Wastewater in Taizhou City. Innovations in Applied Engineering and Technology, 1-7.
15. Deng, T., Huang, M., Xu, K., Lu, Y., Xu, Y., Chen, S., ... & Sun, X. (2024). LEGEND: Identifying Co-expressed Genes in Multimodal Transcriptomic Sequencing Data. bioRxiv, 2024-10.
16. Dang, P., Geng, L., Niu, Z., Chan, M., Yang, W., & Gao, S. (2024). A value-based network analysis for stakeholder engagement through prefabricated construction life cycle: evidence from China. Journal of Civil Engineering and Management, 30(1), 49-66.
17. Louis, E., San-Fabián, E., Díaz-García, M. A., Chiappe, G., & Vergés, J. A. (2017). Are electron affinity and ionization potential intrinsic parameters to predict the electron or hole acceptor character of amorphous molecular materials?. The Journal of Physical Chemistry Letters, 8(11), 2445-2449.
18. Gao, J., Chang, M., & Shen, J. (2017). Comparison of bituminous coal apparent activation energy in different heating rates and oxygen concentrations based on thermo gravimetric analysis. Journal of Thermal Analysis and Calorimetry, 130(2), 1181-1189.
19. Fernández-Navas, N., Shtefan, V., Hantusch, M., & Gebert, A. (2024). Acid treatments of Ti-based metallic glasses for improving corrosion resistance in implant applications. Metals, 14(2), 241.